A Code for Isometric Embeddings of Topological Spheres, With Application to Numerical Relativity

by

Terrence Pierre Jacques

A thesis submitted in partial fulfillment for
Bachelor of Arts in Physics with Honors

Oberlin College
Physics and Astronomy Department

May 2018

"Be remembered for what you do next."

Anonymous

Executive Summary

Black holes are extraordinary objects that have been studied extensively over the last hundred years. Because of their complex nature, however, describing them mathematically results in having to solve several coupled, nonlinear partial differential equations. Numerical relativity was developed to solve these equations using numerical methods.

Once a gravitational field has been computed, either through analytic or numerical means, it must be analyzed. Because gravity is intrinsically tied to geometry, one often wishes to visualize the curvature of some surface by drawing what its shape *would have been* if the surface were a subsurface of familiar Euclidean space (rather than spacetime itself warped in some incomprehensible way). Embedding diagrams allow us to gain this understanding.

In this thesis we motivate the need for constructing embedding diagrams of general surfaces. We then walk the reader through examples of finding embedding diagrams for three different geometries, ending with the difficulty of finding embeddings when axisymmetry isn't present.We present a method previously proposed by Bondarescu et al. in [1], which takes a numerical approach to the problem. We detail our adaption of their approach, and provide test results of our implementation, as well as results on computed data of two black holes coalescing.

Acknowledgements

This project would not have been possible without guidance from Rob Owen. Thank you for inspiring me to delve into the complexity and beauty of General Relativity.

I would like to thank Dan Stinebring for the years of guidance and support. I would not be the physicist I am today without the teachings and experiences you provided me with.

I would also like to thank Peter Stefek for *literally* helping me to make my code 2500 times faster, and for being a pillar of support throughout my years as a physics major.

I would like to give thanks to the Oberlin College Physics and Astronomy department's faculty and staff for pushing me to do the best work I could do. I have undoubtedly become a better physicist because of all of you.

I would like to give thanks to my family for supporting my decision to pursue physics. And most importantly to my parents for providing me with the opportunity to attend Oberlin College.

Finally, I would like to thank Oberlin College for supporting me and other first generation college students.

Contents

List of Figures

Chapter 1

Introduction

A black hole is a knot of pure, vacuum spacetime, the tangle that's left behind after a star collapses under its own weight. Stars usually avoid collapse by employing some kind internal pressure. Normal sized stars rely on thermal pressure, while denser stars resort to electron or neutron degeneracy, using quantum mechanical phenomena to fend against gravity. Nevertheless, there is a point where the star can no longer support itself against the might of gravity, resulting in a violent collapse. The resulting object has a surface, the *horizon*, from which nothing can escape because spacetime there is so tangled that to pass through it objects would have to travel faster than light. Inside this surface, all of the matter that once constituted the star eventually forms into a structure, the *singularity*, where geometry itself has no meaning, at least in classical physics.

Though this structure of strongly-warped spacetime sounds very exotic, we now know that these objects are ubiquitous in our universe, and exist over a wide range of masses. Most normal galaxies have black holes in their cores with masses well over a million times the mass of our sun. One such supermassive black hole, Sagittarius A*, is at the center of our galaxy and has been measured in great detail via the motions of orbiting stars. More distant black holes have been inferred from the x-rays given off by hot gas falling into them. More recent black hole detections have been made through purely gravitational phenomena: the direct measurement of gravitational waves from black hole collisions, by the LIGO-VIRGO collaboration [2].

Black holes exist in astrophysical contexts, usually with matter in their vicinity, and such astrophysical systems can be complicated for a variety of reasons. Systems with neutron stars, for example, are *physically* complicated, since neutron stars are made up of tightly packed neutrons, with their surface surrounded by an atmosphere of relativistic plasma governed by magnetohydrodynamic forces. As a result, simplifying assumptions and approximations are applied to make the problem physically comprehensible. To understand the dynamics of black holes, we therefore consider isolated, stationary astrophysical black holes that are characterized *completely* by only two numbers: their mass and spin. When they are not stationary, it is often because they are "ringing down" to that stationary state in a way that can be well approximated by perturbation theory. The dynamics of the system and spacetime itself, while determined by a large system of nonlinear partial differential equations, can be shown to be well-posed, non-turbulent, and non-chaotic. The system is essentially as simple, physically speaking, as the Maxwellian electrodynamical interaction of two point charges. The difficulty that does exist when analyzing black holes arises from two places. First, the dynamics: while physically simple, arise from the complicated system of nonlinear partial differential equations that need to be solved computationally, and second, the *analysis* of the system is clouded by the fact that one is dealing with the structure of *spacetime itself*, and hence most of our intuitive understanding based on "force", "momentum", and even "shape" become clouded.

Instead of relying on ill-defined Newtonian quantities to understand black hole physics, it is natural to shift focus to the *geometrical* underpinnings that lie at the true foundation of the theory. One way to do this is with a certain kind of diagram called an *embedding diagram*, which will be defined in the next chapter. The pursuit of a general method to find embeddings is the motivation behind this work.

The remainder of this thesis is structured as follows. In chapter 2, we define embedding diagrams and motivate their use for describing the geometry of curved spacetime. In chapter 3, we describe an approach to finding horizon embeddings that previously existed in the literature, and our improvements upon it. In chapter 4 we describe our implementation of this method in numerical code, with examples of specific test cases. In chapter 5, we present our analysis of a physical and historically-relevant case, the numerical simulation (by the SXS collaboration) [3]

of the first measured gravitational-wave event, GW150914 [2]. In chapter 5 we summarize and discuss remaining questions and the prospects for future work.

Chapter 2

Motivation

General Relativity is the physics of *geometry*. Geometry is concerned with the relationship between points in space (or "events" in spacetime), and with the curves that connect them, the surfaces that connect curves, the volumes that connect surfaces and so on. The foundation of geometry is the concept of distance. In the Euclidean plane, the distance between two points is given by

$$(\Delta s)^2 = (\Delta x)^2 + (\Delta y)^2, \tag{2.1}$$

which represents the length of the *straight line* path between two points. It can be shown that any non-straight path between these two points necessarily has a length that is longer than this Δs. To define the length of an *arbitrary* path, one must use a *differential* distance measure,

$$ds^2 = dx^2 + dy^2, \tag{2.2}$$

and define the length as an integral. Such a differential distance measure is useful when one does not wish to use Cartesian coordinates (which might not exist in a curved spacetime). For example, the differential distance on the Euclidean plane, in polar coordinates, is given by

$$ds^2 = dr^2 + r^2 d\theta^2. \tag{2.3}$$

The differential distance measure also has the advantage that it can can even be used on non-flat surfaces. On the surface of a sphere the distance measure can be defined as

$$ds^2 = r^2 d\theta^2 + r^2 \sin^2\theta d\phi^2. \tag{2.4}$$

This distance measure represents a fundamentally different system of geometry than the measures above for the Euclidean plane. In this geometry, for example, the sum of interior angles in a triangle is greater than 180°. These differential distance measures are also known as line elements. If we were not already familiar with these line elements, however, it would be a nontrivial undertaking to *show* that this line element represents a fundamentally different system of geometry, as opposed to simply looking different because of different coordinate choices.

Extending further, thanks to arguments of Bernhard Riemann in his *Habilitazion*, ‘Uber die Hypothesen, welche der Geometrie zu Grunde liegen’ [4], one can construct very general systems of non-Euclidean geometry with a general quadratic line element that we write compactly as

$$ds^2 = g_{\alpha\beta} dx^\alpha dx^\beta. \tag{2.5}$$

Here the raised indices α and β are not exponents, and in spacetime they vary from 0 to 3, where, usually, $x^0 = t$ and x^i are the three spatial coordinates. By convention, any index that appears two times in a term, once low and once high, is implicitly taken to be summed over that index. Hence equation 2.5 has an implicit double sum, once over α from 0 to 3, and once over β from 0 to 3. $g_{\alpha\beta}$, a symmetric square matrix that varies from point to point, is known as the metric, which encodes the geometry of the surface.

Euclidean space is known as flat space because none of the coefficients for the line element describing it depend on coordinates. The metric for Euclidean space is then defined as

$$ds^2 = dx^2 + dy^2 + dz^2. \tag{2.6}$$

Minkowski spacetime is defined as a Euclidean surface with a time dimension, with its line element defined as

$$ds^2 = -dt^2 + dx^2 + dy^2 + dz^2, \tag{2.7}$$

in c =1 units. The geometry of Minkowski spacetime is independent of coordinates, so in a similar sense to Euclidean space it also flat, and is typically referred to as flat spacetime.

In principle if one took *any two* families of curves, the curves can be used to represent level-sets of some general coordinate system in the Euclidean plane, and the line element can be written in terms of those coordinates. Therefore, there are *infinitely many* coordinate systems in the Euclidean plane. The Cartesian coordinates are singled out by the fact that the line element takes the very simple form of equation 2.2, with no coordinate-dependent coefficients. In an intrinsically-curved geometry such as the one specified by equation 2.4, or in spacetimes with nonzero gravitational fields, it can be shown that there *are no coordinate systems* with this special property. This becomes a problem when trying to describe the "shape" of objects, because when typically thinking about their shape, one is implicitly assuming that the body is represented in these preferred Cartesian coordinates. When there are no preferred "Cartesian" coordinate systems, the visual shape of an object becomes completely undefined. This difficulty can be addressed, in many cases, using the mathematical technique of *isometric embedding*.

Embeddings can help to visualize and understand the geometry of a surface. During the adolescence of general relativity embeddings were found to be illuminating when considering the curvature of spacetime. Today they are an essential part to understanding what geometry means, and provide powerful insights into the dynamics of black holes. A plethora of texts, both elementary and advanced, involve discussions and analyses related to embeddings, e.g. [5, 6] and references therein.

As an example of the concept of an embedding, consider a very curious ant, who forgot his glasses at home, standing at the stem of a fruit with a smooth glossy skin. Is there any experiment the ant can do to infer whether the fruit is a *pear* or an *apple*? The ant could walk some number of paces directly away from the stem in a straight line, and mark that number of paces down in his little ant lab notebook, and label it "radius." The ant would then mark his place on the surface and walk

around in a purely polar direction (he was clever enough to tie a string to the stem at the start of the experiment) until he comes back to where he started. He marks down that number of paces as the "circumference." If the ant then compares those numbers and notes that $C < 2\pi R$, then he would immediately infer that the surface on which he did the measurements is curved, since these quantities should be equal on a flat surface. Moreover, if he repeats the experiment for many radii, and finds that for some significant variation in R the circumference changes very little, then he could infer that he is on some extended region of roughly cylindrical shape, as near the stem of a *pear*. If the circumference, while still less than $2\pi R$ varies more rapidly with R, then the ant might infer that the surface is shaped more like an apple. With enough measurements, the ant could even *infer the exact shape* of the surface in three-dimensional Euclidean space. *That* is the embedding problem. In general relativity, one can take the intrinsic geometry on an arbitrary 2-dimensional surface, suppose that the surface is a surface in a Euclidean space, and find what the shape of the object would have to be in order to be consistent with what is known about the 2-dimensional geometry.

Finding an embedding for the horizon of a black hole is useful because it allows us to visually confirm theorized characteristics of this surface. This is the main motivation of the work presented, but another goal of this research was to find a method to find embeddings to calculate the energy [7] that is inside the surface, and from there apply tests to confirm the Hoop Conjecture. The conjecture states that any object whose surface cannot be enclosed by some rotating hoop about some common origin will never collapse into a black hole [8]. Using a generalized method for finding embeddings, this work can also confirm the results of [9], namely that the object resulting from the merging of two black holes will settle down to the standard 'Kerr' black hole solution, in an unambiguous sense.

Before moving on, it is worth mentioning what is meant by curvature. A full description of curvature in arbitrary dimensions is beyond the scope of this thesis, however for the two-dimensional surfaces of most interest in this thesis a simple concept of curvature exists, due to Gauss [10]. One can show that at any point on a smooth two-dimensional surface, there are two special axes (called "principal axes") along which a path would need to be the most curved in order to follow the surface. Specifically, if one parametrizes the surface in Cartesian coordinates as $z(x, y)$ (after rotating the surface to make it locally horizontal at the point under consideration), then the principal axes are the eigen-directions of the matrix

$\partial_i \partial_j z(x, y)$, and the "principal curvatures" κ_1 and κ_2 are the second derivatives of z along these special directions. The principal curvatures are not "intrinsic," meaning they are not individually measurable just from measurements on the surface. However their *product*, called the *Gaussian curvature* $K = \kappa_1 \kappa_2$ *is* intrinsic to the surface, and therefore would be measurable by the ant in the above parable (for example). The Gaussian curvature is positive either if both principal curvatures are positive (as in a bowl), or if both are negative (an inverted bowl); the Gaussian curvature is negative if the two principal curvatures have opposite sign (as in a saddle point or a trumpet flare).

One difficulty with the embedding process is that sometimes an embedding in Euclidean space simply doesn't exist. The physical horizon of a black hole is embedded in a curved four-dimensional geometry, but this does not imply that an embedding exists in flat three-dimensional geometry. In fact, even the horizon of a simple isolated rotating black hole cannot be embedded in $\mathbb{E}^3$ if the spin parameter of the hole is too high. This turns out to be due to the fact that the Gaussian curvature becomes negative at the poles, which (along with axisymmetry) requires them to flare up into a trumpet shape that is incompatible with the smoothness of the geometry at the poles [6]. We will confirm this behavior with our code in Chapter 4. If a global embedding does not exist, however, it may still be possible for "patches" of the horizon to be individually embeddable.

In the remainder of this chapter we will work through three examples of embeddings. The first we consider is perhaps the most iconic embedding problem, called the *Einstein Rosen Bridge*. Consider the simplest black hole solution, with zero charge, zero spin, and no tidal structure, called the *Schwarzschild* black hole. In standard coordinates the line element is

$$ds^2 = -\left(1 - \frac{2M}{r}\right) dt^2 + \frac{1}{1 - \frac{2M}{r}} dr^2 + r^2 d\theta^2 + r^2 \sin^2\theta d\phi^2, \tag{2.8}$$

where M is a parameter representing the mass of the hole, t is the time coordinate, and (r, θ, ϕ) are (roughly speaking) spherical coordinates (with the necessary condition $r > 2M$, to avoid a blowup of g_{rr}). The horizon of this spacetime turns out to be, intrinsically, a perfect sphere, so its embedding is not particularly interesting. Instead, we embed a "spatial slice," $t = 0$, $\theta = \pi/2$, on which the line element becomes

$$ds^2 = \frac{1}{1 - \frac{2M}{r}} dr^2 + r^2 d\phi^2. \tag{2.9}$$

Here we can note that equation 2.9 doesn't depend on ϕ, meaning that for any ϕ, the geometry remains the same for ϕ + constant. This fact indicates that the surface has axisymmetry. Given this condition, we may as well define our embedded surface in cylindrical coordinates (z, ρ, ψ). Therefore, in Euclidean space have

$$z = z(r, \phi), \rho = \rho(r, \phi), \psi = \psi(r, \phi). \tag{2.10}$$

The metric for Euclidean space expressed in cylindrical coordinates reads

$$ds^2 = d\rho^2 + \rho^2 d\psi^2 + dz^2. \tag{2.11}$$

Now, because the original surface has axisymmetry, so too must our embedded surface, implying that

$$z = z(r), \rho = \rho(r), \psi = \phi. \tag{2.12}$$

If our embedded surface is to have the same intrinsic geometry as our original surface, we must enforce that equation 2.11 equals equation 2.9 at all points in space. After some manipulation, we then have

$$\left[\left(\frac{dz}{dr} \right)^2 + \left(\frac{d\rho}{dr} \right)^2 \right] dr^2 + \rho^2 d\phi^2 = \frac{1}{1 - \frac{2M}{r}} dr^2 + r^2 d\phi^2, \tag{2.13}$$

implying that

$$\rho^2 = r^2, \tag{2.14}$$

and

$$\left[\left(\frac{dz}{dr} \right)^2 + \left(\frac{d\rho}{dr} \right)^2 \right] = \frac{1}{1 - \frac{2M}{r}}. \tag{2.15}$$

Solving these equation, we thus have

$$\rho = r, z = \pm 2\sqrt{2M(r-2M)}. \tag{2.16}$$

Here we note that the positive root corresponds to the standard black hole exterior, while the negative root corresponds to a separate region of spacetime. The throat between them, at $r = 2M$, is a (non-traversable) bridge between these two regions. Figure 2.1 are plots of the embedded surfaces.

FIGURE 2.1: Einstein Rosen Bridge embedding diagrams. The left plot is z with the positive root, and the right plot is with the negative root. The plots are connected via the bridge that passes through $z = 0$.

The next surface we will embed is defined by the line element for a sphere stretched out in the z-direction, or a prolate spheroid. The line element is

$$ds^2 = a^2[1 + \epsilon \sin^2\theta]d\theta^2 + a^2 \sin^2\theta d\phi^2, \tag{2.17}$$

where a is the radius of the sphere and ϵ is the eccentricity. Here we note again that the original surface has axisymmetry, so we can follow the same procedure used in the previous example, with the change to cartesian coordinates (x, y, z) for convenience. Doing so yields

$$x = a \sin\theta \cos\phi, y = a \sin\theta \sin\phi, z = a\sqrt{1+\epsilon}\cos\theta. \tag{2.18}$$

Figure 2.2 are plots of various eccentricities.

Our last example involves the line element

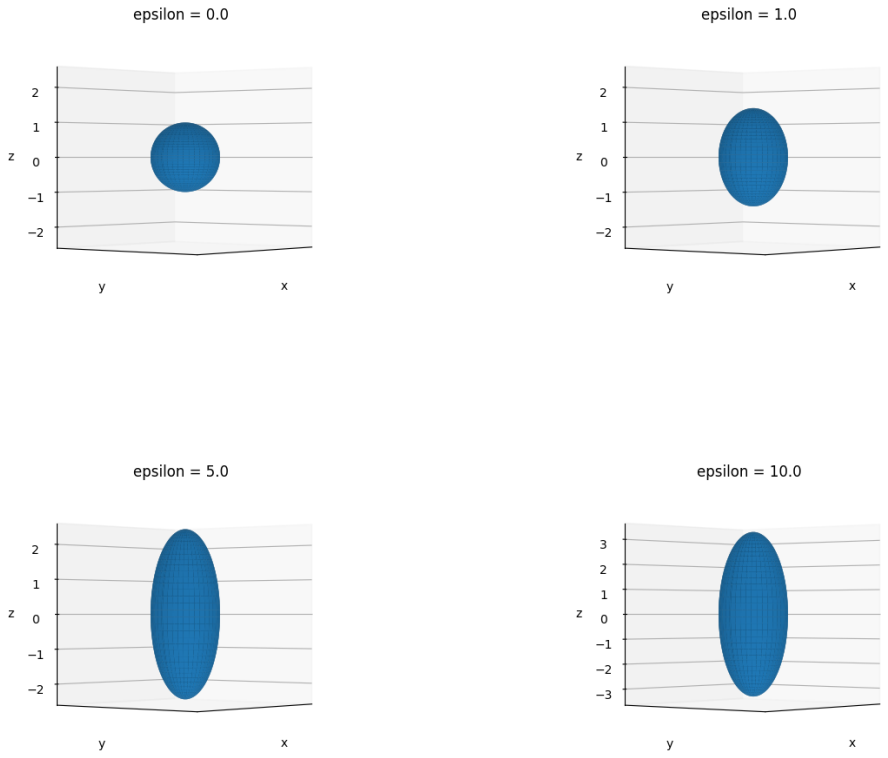

FIGURE 2.2: Plots of the prolate spheroid for various eccentricities. Note that the lower right plot has its z axis scaled differently than the others.

$$ds^2 = a^2[1 + \epsilon \cos^2\theta \cos^2\phi]d\theta^2 + a^2 \sin^2\theta[1 + \epsilon \sin^2\phi]d\phi^2 - \frac{1}{2}a^2\epsilon \sin 2\theta \sin 2\phi d\theta d\phi. \tag{2.19}$$

Unlike the last two examples, because equation 2.19 does depend on ϕ we cannot assume axisymmetry, which results in the system of equations

$$x_{,\theta}^2 + y_{,\theta}^2 + z_{,\theta}^2 = a^2[1 + \epsilon \cos^2\theta \cos^2\phi], \tag{2.20}$$

$$x_{,\phi}^2 + y_{,\phi}^2 + z_{,\phi}^2 = a^2 \sin^2\theta[1 + \epsilon \sin^2\phi], \tag{2.21}$$

$$2(x_{,\theta}x_{,\phi} + y_{,\theta}y_{,\phi} + z_{,\theta}z_{,\phi}) = -\frac{1}{2}a^2\epsilon \sin 2\theta \sin 2\phi, \tag{2.22}$$

where the subscripted commas represent partial derivatives, with respect to θ or ϕ. If this system looks near impossible to solve, it's because it is, more or less. This is a system of nonlinear, first order partial differential equations. To make matters worse, this was the metric for a prolate spheroid, but with the eccentricity applied along the x axis instead of the z axis. The intrinsic geometry is the same as the last example, but through a rotation about the axes the embedding problem has become far more difficult.

There is a method for finding the embedding for two dimensional surfaces in general, given that the surface does not posses negative guassian curvature. One can transform this set of equations to a single nonlinear second order partial differential equation using the Darboux equation [11]. Even so, numerical methods must be applied to solve this equation and find an embedding. The work here also uses a numerical method to find an embedding, but ours is far less computationally complex and less expensive.

In binary black hole merger simulations, we desire the ability to visualize the surfaces at each time step. However, tidal interactions between the black holes make them non-axisymmetric before and immediately after merging, making the embedding very complex, like the non-axisymmetric spheroid described above. Hence, we need a general method to solve such embedding problems for closed surfaces numerically. That will be the topic of the next chapter.

Chapter 3

Method

In a 2002 paper [1] Bondarescu et al. transform the problem of finding embeddings of black holes into an optimization problem. Here I will outline their approach and highlight the key aspects of their method, including the minimization algorithm the group used.

The motivation behind their method is that visualizing the surfaces of black holes only using information from the simulation derived coordinate space data can be unhelpful, as a single physical system will have representations in different coordinate systems, and in fact two different physical systems can have similar coordinate representations. The authors note, however, that while local embeddings of two dimensional surface always exists, global embeddings may easily not, such as closed surfaces with negative Gaussian curvature.

In general, finding these embeddings, if they do exist, can be difficult if axisymmetry is not present. As mentioned earlier, the Darboux equation is one method used for finding an embedding in general, but if the surface has a nontrivial shape with regions of varying sorts of curvature, then the method becomes quite difficult to use, because the character of the involved partial differential equations (elliptic versus hyperbolic) varies from point to point according to the local value of the Gaussian curvature.

For their method, they first make a small set of assumptions to build up the mathematical motivation behind their formulation. The first assumption is that since black holes have spherical topology, meaning surfaces that have similar structure to perfect spheres, the metric defining their three - dimensional surface can be

given in spherical coordinates that enclose some origin. The second is that these surfaces are star shaped. This means that any line from the origin intersects the surface at only one point. Therefore, points on the surface can be represented with just the coordinates (θ, ϕ), without a need to specify the radial coordinate.

If the embedded surface does exist, then it is safe to assume that it can also be represented using spherical coordinates, namely (r_e, θ_e, ϕ_e) in flat space. One cannot, however, assume that there is a direct mapping between coordinates (θ, ϕ) in the coordinate space and the coordinates (θ_e, ϕ_e) in flat space, since there could be some nontrivial, nonlinear transformation between them. Thus, in general the flat space coordinates are functions

$$r_e = r_e(\theta, \phi), \theta_e = (\theta, \phi), \phi_e = (\theta, \phi). \tag{3.1}$$

Here we note that (θ, ϕ) will still be a well-behaved coordinate system in flat space. Since our original surface has spherical topology and this coordinate system defined each point uniquely, our embedded surface will also have spherical topology, and so this inherited coordinate system should also uniquely define points on this surface in flat space. Therefore, the embedded surface can be expressed in two different coordinate systems; the flat space coordinates and the inherited coordinates.

The coordinates r_e, θ_e, ϕ_e are useful because they represent the *Euclidean* geometry of the background space. Hence, we know that the line element, in these coordinates is

$$ds^2 = dr_e^2 + r_e^2 d\theta_e^2 + r_e^2 \sin^2 \theta_e d\phi_e^2. \tag{3.2}$$

This, however, is the line element along an arbitrary curve in the three-dimensional Euclidean space. If we wish to localize this line element to our surface, we note that we are presuming $r_e = r_e(\theta, \phi)$, $\theta_e = \theta_e(\theta, \phi)$, $\phi_e = \phi_e(\theta, \phi)$. The differentials can thus be expanded as

$$dr_e = \frac{\partial r_e}{\partial \theta} d\theta + \frac{\partial r_e}{\partial \phi} d\phi, \tag{3.3}$$

and similar for θ_e and ϕ_e. After some tedious simplification, the above line element can then be put in the form

$$ds^2 = G^e_{\theta\theta} d\theta^2 + G^e_{\phi\phi} d\phi^2 + 2G^e_{\theta\phi} d\theta d\phi, \tag{3.4}$$

where the coefficients $G^e_{\theta\theta}$, $G^e_{\phi\phi}$, and $G^e_{\theta\phi}$ are purely functions of the surface coordinates (θ, ϕ). Ensuring that this equals the known intrinsic line element

$$ds^2 = G_{\theta\theta} d\theta^2 + G_{\phi\phi} d\phi^2 + 2G_{\theta\phi} d\theta d\phi, \tag{3.5}$$

simply means equating the coefficients

$$G_{\theta\theta} = G^e_{\theta\theta}, G_{\phi\phi} = G^e_{\phi\phi}, G_{\phi\theta} = G^e_{\phi\theta}. \tag{3.6}$$

The problem now is to find the metric components for the embedded surface. In general, without assuming axisymmetry, the transformations between (r_e, ϕ_e, θ_e) and (θ, ϕ) are given by

$$\theta_e(\theta, \phi) = \theta + \sum_{n=0}^{\infty} b_{n0} \sin n\theta + \sum_{n=1}^{\infty} \sum_{m=1}^{\infty} b_{nm} \sin n\theta \sin m\phi. \tag{3.7}$$

$$\phi_e(\theta, \phi) = \phi + c_{00} + \sum_{n=1}^{\infty} c_{n0} \sin n\theta + \sum_{m=1}^{\infty} c_{0m} \sin m\phi + \sum_{n=1}^{\infty} \sum_{m=1}^{\infty} c_{nm} \sin n\theta \sin m\phi. \tag{3.8}$$

$$r_e(\theta, \phi) = \sum_{l=0}^{\infty} \sum_{m=-l}^{l} \sqrt{4\pi} a_{lm} Y_{lm}(\theta, \phi), \tag{3.9}$$

where $Y_{lm}(\theta, \phi)$ are the spherical harmonics, defined as

$$Y_{lm}(\theta, \phi) = \sqrt{\frac{(l-m)!(2l+1)}{4\pi(l+m)!}} e^{im\phi} P^m_l(\cos\theta), \tag{3.10}$$

and $P^m_l(\cos\theta)$ are the associated legendre functions.

The second term in equation 3.7 is used for a generic axisymmetric mapping and the third term is used for when axisymmetry is not assumed. The second and third

terms of equation 3.8 account for a possible rigid twist between the coordinate systems, and the last two terms are responsible for a general dependence on θ and ϕ. In equation 3.10 $Y_{lm}(\theta, \phi)$ are the spherical harmonics for numbers l and m, where $l \geq |m| \geq 0$.

Given these transformations, the authors then consider four points on the embedded surface, namely $P_1 = (\theta, \phi)$, $P_2 = (\theta + \delta\theta, \phi)$, $P_3 = (\theta, \phi + \delta\phi)$, $P_4 = (\theta + \delta\theta, \phi + \delta\phi)$. The metric components can then be calculated using the square distances between these points.

$$(\overline{P_1P_2})^2 = G^e_{\theta\theta} d\theta^2. \tag{3.11}$$

$$(\overline{P_1P_3})^2 = G^e_{\phi\phi} d\phi^2. \tag{3.12}$$

$$(\overline{P_1P_4})^2 = G^e_{\theta\theta} d\theta^2 + G^e_{\phi\phi} d\phi^2 + 2G^e_{\theta\phi} d\theta d\phi. \tag{3.13}$$

The crucial observation here is that with G^e expressed as transformations via equations 3.11, 3.12, and 3.13 and the subsequent manipulations in equations 3.7, 3.8, and 3.9, at any point (θ, ϕ), G^e is uniquely determined by the coefficients a_{lm}, b_{nm}, and c_{nm}. If one then considered the space of these coefficients as some vector space V, then any point in V would represent some embedded surface.

If $G = G^e$, then our embedded surface will have the same intrinsic geometry as the original surface. With this in mind, the authors define the function F with domain V such that

$$F = \int_{\theta=0}^{\pi} \int_{\phi=0}^{2\pi} [(G_{\theta\theta}(\theta,\phi) - G^e_{\theta\theta}(\theta,\phi))^2 + (G_{\phi\phi}(\theta,\phi) - G^e_{\phi\phi}(\theta,\phi))^2 + (G_{\theta\phi}(\theta,\phi) - G^e_{\theta\phi}(\theta,\phi))^2] d\theta d\phi \tag{3.14}$$

F may be considered as a residual function, summing over all the differences between the surfaces. With F in this form, one could imagine having some surface in V on which F is defined, with some point P where $F = 0$. This point corresponds to the two geometries being identical.

The point P will lie at some global minimum for F, and thus finding the correct embedding corresponds to finding P, hence an optimization problem. If one could find the global minimum of F, then one would have found the embedding of the original surface.

To find the exact location of a global minimum on F, one would have to push the number of coefficients to infinity. As a result, in the process of finding P one would need to settle for a point "close" to the minimum, within some desired tolerance. The authors use Powell's algorithm [12] as their optimization method, but note that others may be perform better. They also note that they have seen the algorithm settle on different local minima. Because there is no way to distinguish between local and global minima without exploring out to infinity, to find the best minimum they care for, for each embedding search the authors started with a small number of coefficients and slowly increased them until F achieved some specified tolerance.

The authors comment that such a process for finding embeddings can be long, although they don't mention any specific runtimes. This is most likely due to the nature of Powell's method.

Powell's method is a conjugate direction method that tries to find global optima. In some N dimensional vector space the algorithm takes an initial point P_0 and from there goes along each of the vector space's basis vectors $\mathbf{e_i}$ and minimizes along each of these directions. This method does not use or compute the gradient, but instead may use some other minimization method along $\mathbf{e_i}$, such as binary search. The authors do not mention what line minimization method they used, but those such as binary search will frequently get stuck in local minima. Overall, however, this algorithm will be fairly slow for high orders of N. This slowdown in their method is the likely cause of the authors having to increase their number of parameters one by one.

The work presented here expands on that of Bondarescu et al. We consider the same formalism, employ the same assumptions, but we diverge from their work in implementation.

Instead of using the coordinate transformation from (θ, ϕ) to (r_e, θ_e, ϕ_e), we transform from the inherited coordinate system to cartesian coordinates (X_e, Y_e, Z_e) through the equations

$$X_e(\theta,\phi) = \sum_{a=0}^{\infty} x_a \mathcal{Y}_a(\theta,\phi), \tag{3.15}$$

$$Y_e(\theta,\phi) = \sum_{a=0}^{\infty} y_a \mathcal{Y}_a(\theta,\phi), \tag{3.16}$$

$$Z_e(\theta,\phi) = \sum_{a=0}^{\infty} z_a \mathcal{Y}_a(\theta,\phi), \tag{3.17}$$

where x_a, y_a, and z_a are numerical coefficients, and $\mathcal{Y}_a(\theta,\phi)$ are the spherical harmonics for some l and m, which are defined as functions of a:

$$l = \lfloor \sqrt{a} \rfloor, \tag{3.18}$$

and

$$m = a - l^2 - l. \tag{3.19}$$

We can construct the components of G^e by using the following procedure. For a surface with its metric defined in coordinates (u, v), the line element may be written as

$$ds^2 = Adu^2 + 2Bdudv + Cdv^2, \tag{3.20}$$

where A, B, and C are components of the surface's metric. We can then introduce embedding functions $X(u, v)$, $Y(u, v)$, and $Z(u, v)$ that satisfy

$$ds^2 = dX^2 + dY^2 + dZ^2. \tag{3.21}$$

Setting these equations equal, we see that incremental changes in X, Y, and Z must also yield incremental changes in u and v. Therefore, we must have

$$A = (\partial_u X)^2 + (\partial_u Y)^2 + (\partial_u Z)^2, \tag{3.22}$$

$$C = (\partial_v X)^2 + (\partial_v Y)^2 + (\partial_v Z)^2 \,, \tag{3.23}$$

$$B = \partial_u X \partial_v X + \partial_u Y \partial_v Y + \partial_u Z \partial_v Z. \tag{3.24}$$

In our method of embedding, where $(u, v) = (\theta, \phi)$, we have $A = G^e_{\theta\theta}$, $C = G^e_{\phi\phi}$, and $B = G^e_{\theta\phi}$.

One problem with the minimization residual F defined in equation 3.14 is that it does not account for the behavior of the metric coefficients near the poles. One can show that on any surface that is smooth near the poles, the metric coefficient $G_{\phi\phi}$ is naturally proportional to $\sin^2\theta$ as the pole is approached, and similarly $G_{\theta\phi}$ is proportional to $\sin\theta$. Therefore, errors in the embedding near the pole could be *hidden* by the fact that the functions are naturally smaller there. To correct for this, we divide by appropriate factors of $\sin\theta$ derived from a more sophisticated geometric treatment of the residual function. The resulting residual is

$$R = \int_{\theta=0}^{\pi} \int_{\phi=0}^{2\pi} [\sin\theta (G_{\theta\theta} - G^e_{\theta\theta})^2 + \frac{1}{\sin^3\theta}(G_{\phi\phi} - G^e_{\phi\phi})^2 + \frac{2}{\sin\theta}(G_{\theta\phi} - G^e_{\theta\phi})^2] d\theta d\phi. \tag{3.25}$$

We introduce the implementation described above, representing all coordinates via spherical harmonic expansion, for two reasons. The first is that we can express the change of coordinates in a much tidier fashion, utilizing the completeness theorem of the spherical harmonics.

Not only do the spherical harmonics offer solutions to Laplace's equation, but they also form a complete and orthogonal set. This is a similar idea to using a Fourier series to approximate a periodic function.

In a function space, a function $f(x)$ may be represented as a linear combination of linearly independent basis functions of that space. These basis functions may be used if they form a complete set. The set is complete if all possible functions in that function space may be represented as linear combinations of the basis functions.

In the same way, one can construct any smooth function on a topological sphere using a combination of spherical harmonics. The spherical harmonics are particularly convenient because they form an orthogonal basis in the function space, meaning

$$\int\int \mathcal{Y}^{\star}_{\alpha}(\theta,\phi)\mathcal{Y}_{\beta}(\theta,\phi)\sin\theta d\theta d\phi = \delta_{\alpha\beta} \tag{3.26}$$

As a result, we can approximate the transformations of equations as series of spherical harmonics since both surfaces will have identical geometry.

The second reason we introduce this implementation is that it allows us to explore V in a more efficient manner. In general, when trying to find optima for some scalar function $f(\mathbf{v})$, it is a safe bet to use a method that employs the function's gradient in some way, given that it is continuous and its partial derivatives exist and are continuous. With equations 3.7, 3.8, and 3.9, if one could take the partial derivatives of F with respect to each coefficient, then one could use these to construct F's gradient, and follow it to optimality. In principle this could be done, but it would result in quite an unwieldy set of equations to deal with. We chose our implementation so that constructing the gradient of R would be straightforward. And indeed, components of the gradient of R take the the forms

$$\begin{aligned}\frac{\partial R}{\partial x_a} = \int_{\theta=0}^{\pi}\int_{\phi=0}^{2\pi} & 4(G_{\theta\theta}-G^{e}_{\theta\theta})\partial_{\theta}X\partial_{\theta}\mathcal{Y}_a(\theta,\phi) + 4(G_{\phi\phi}-G^{e}_{\phi\phi})\partial_{\phi}X\partial_{\phi}\mathcal{Y}_a(\theta,\phi) \\ & + 2(G_{\theta\phi}-G^{e}_{\theta\phi})[\partial_{\phi}X\partial_{\theta}\mathcal{Y}_a(\theta,\phi) + \partial_{\theta}X\partial_{\phi}\mathcal{Y}_a(\theta,\phi)]d\theta d\phi, \end{aligned} \tag{3.27}$$

$$\begin{aligned}\frac{\partial R}{\partial y_a} = \int_{\theta=0}^{\pi}\int_{\phi=0}^{2\pi} & 4(G_{\theta\theta}-G^{e}_{\theta\theta})\partial_{\theta}Y\partial_{\theta}\mathcal{Y}_a(\theta,\phi) + 4(G_{\phi\phi}-G^{e}_{\phi\phi})\partial_{\phi}Y\partial_{\phi}\mathcal{Y}_a(\theta,\phi) \\ & + 2(G_{\theta\phi}-G^{e}_{\theta\phi})[\partial_{\phi}Y\partial_{\theta}\mathcal{Y}_a(\theta,\phi) + \partial_{\theta}Y\partial_{\phi}\mathcal{Y}_a(\theta,\phi)]d\theta d\phi, \end{aligned} \tag{3.28}$$

$$\frac{\partial R}{\partial z_a} = \int_{\theta=0}^{\pi}\int_{\phi=0}^{2\pi} 4(G_{\theta\theta} - G^e_{\theta\theta})\partial_\theta Z \partial_\theta \mathcal{Y}_a(\theta,\phi) + 4(G_{\phi\phi} - G^e_{\phi\phi})\partial_\phi Z \partial_\phi \mathcal{Y}_a(\theta,\phi) + 2(G_{\theta\phi} - G^e_{\theta\phi})[\partial_\phi Z \partial_\theta \mathcal{Y}_a(\theta,\phi) + \partial_\theta Z \partial_\phi \mathcal{Y}_a(\theta,\phi)] d\theta d\phi. \quad (3.29)$$

Note that each partial differential equation is different for every index a. With these quantities, we can construct the gradient by considering these partial derivatives to be components of a single vector. If we considered the sums in equations 3.15, 3.16, and 3.17 to terminate at N, then V would be $3N$ dimensional, and the gradient of R in V would thus be

$$\vec{\nabla} R = \begin{pmatrix} \frac{\partial R}{\partial x_0} \\ \vdots \\ \frac{\partial R}{\partial x_N} \\ \frac{\partial R}{\partial y_0} \\ \vdots \\ \frac{\partial R}{\partial y_N} \\ \frac{\partial R}{\partial z_0} \\ \vdots \\ \frac{\partial R}{\partial z_N} \end{pmatrix}. \quad (3.30)$$

Using this vector we can then direct the function to decrease along it, trying to locate the global minimum.

Chapter 4

Implementation and Testing

In our implementation, our main scripts were written in python, using the NumPy library. We used NumPy for it's speed in matrix manipulations, enabling us to use dynamic programming to calculate everything in bulk.

To calculate the spherical harmonic for any given index a, we used the array-based spherical harmonics function in the C GNU Scientific Library, gsl_sf_legendre_deriv_alt_array, which calculates all the spherical harmonics and their derivatives. We used the Cython library to wrap this C code into a module in Python. This was done to give us more flexibility and control in our calculations, and resulted in considerable speedups in comparison to using pre-packed Python routines.

We used the Truncated Newton method algorithm [13–15] of the minimization package within the SciPy library. The algorithm uses a conjugate gradient sub-algorithm to solve the system of equations for some vector $\mathbf{x}$ for some function $f(\mathbf{x})$

$$\vec{\nabla} f(\mathbf{x}) = 0, \tag{4.1}$$

which would represent optimality. This is done by iteratively solving for step-sizes to take along the gradient, governed by

$$\nabla^2 f(\mathbf{x}_k) p_k = -\vec{\nabla} f(\mathbf{x}_k), \tag{4.2}$$

where p_k is the stepsize at the kth iteration.

To begin the minimization process, an initial guess must first be given for values of the considered coefficients, as well as the total number of coefficients. Starting with all coefficients equaling to zero yields a single point at the origin, while starting with all the coefficients equal to one yields a spiky, complex shape. As a first initial guess, it is sensible to start with a perfect sphere, and allow the algorithm to make perturbations on the surface to fit the surface we are trying to converge to. A perfect sphere corresponds to $x_3 = r$, $y_1 = r$, and $z_2 = r$, where r is the radius.

For each embedding problem, we must choose the total number of coefficients $3N$ we wish to consider. The more coefficients we use, the larger our parameter space becomes (in terms of dimensionality), and thus the more accurate our embedding will be. The trade off, however, will be the computation time. As N increases, the array operations in our algorithm take up more time and resources. For most cases, however, when we increase N we also acquire a smaller R.

There were times when although we had higher N, the algorithm would get stuck in local minima with solutions of nonzero coefficients in the higher order spherical harmonics, resulting in higher R than when N was lower. To help prevent this, we would keep N fairly low, $N = 100$, and increase it slightly to test if a smaller R could be found. In finding embeddings for simulated data we found that adaptively increasing N yielded better results at each time step than keeping N the same for all surfaces.

We also experimented with a penalty system to nudge the algorithm away from adjusting the higher order terms too much. This turned out to be of little help because our residual function would attain very large values, and using a penalty system to make these values even greater in the evaluation of R resulted in runtime errors.

We conducted three sets of tests to discern the behavior of our implementation, and test for inaccuracies or bugs in our code. The first test was to find the embedding for a prolate spheroid, with its principal axes rotated from the xyz axes, given by the metric

$$ds^2 = a^2[1+\epsilon\cos^2(\theta)\cos^2(\phi)]d\theta^2+a^2\sin^2(\theta)[1+\epsilon\sin^2(\phi)]d\phi^2-\frac{1}{2}a^2\epsilon\sin(2\theta)\sin(2\phi)d\theta d\phi \tag{4.3}$$

This test provided mixed results. When trying to solve the embedding with a fixed number of parameters, the residual function would often get stuck in local minima, which did not have the basic shape of prolate spheroids. Instead, we tried an iterative approach to finding the embedding. Starting with zero eccentricity (a perfect sphere), at each time step the residual function was evaluated, and if it was above some threshold the minimization routine would be applied. If the residual was below the threshold, then the eccentricity would be increased slightly, and so on, using the values of the previous set of parameters as the new initial guess. We found that this method did allow us to keep the residual at around 10^{-5}, but took up far more computational time, on the order of hours. In principle, if we allowed the code to run for a month or two, we would eventually find the embeddings for prolate spheroids of various eccentricities.

The second test was to find the embedding for the geometry of a peanut, given by the metric

$$ds^2 = a^2 d\theta^2 + a^2[\sin(\theta)(1 - 0.75\sin^2(\theta))]^2 d\phi^2, \tag{4.4}$$

where the parameter a is a scaling factor for the entire size of the peanut [16]. The algorithm finds the embedding in a straightforward fashion, without getting stuck in any local minima. The scaling factor does have the effect that the initial starting point has increased error from the original surface with the increase of a, and the end result of the minimization is considerably worse, but at $a = 1$, the algorithm converges to $R = 10^{-6}$. It is still unclear why our algorithm exhibits this behavior The resulting embedding diagram is displayed in figure 4.1.

The third test was finding the embedding for a zero charge, rotating black hole, varying the angular momentum parameter for each embedding. Bondarescu et al. found that their residual function increased exponentially as they increased the angular momentum parameter a past $\sqrt{3}/2$. This value is where the embedding no longer exists in Euclidean space, because the poles begin to have negative gaussian curvature [6]. We also observed this behavior, validating the accuracy of our method. The results are shown in figure 4.2. In our implementation we also observed that the algorithm yields surfaces with either inward pointing or outward pointing dips on the poles of the object. An example is shown in figure 4.4. Below the cut off value, we were able to find embeddings with $R = 10^{-8}$ or lower. This range of residual values seems to be where we can have the most

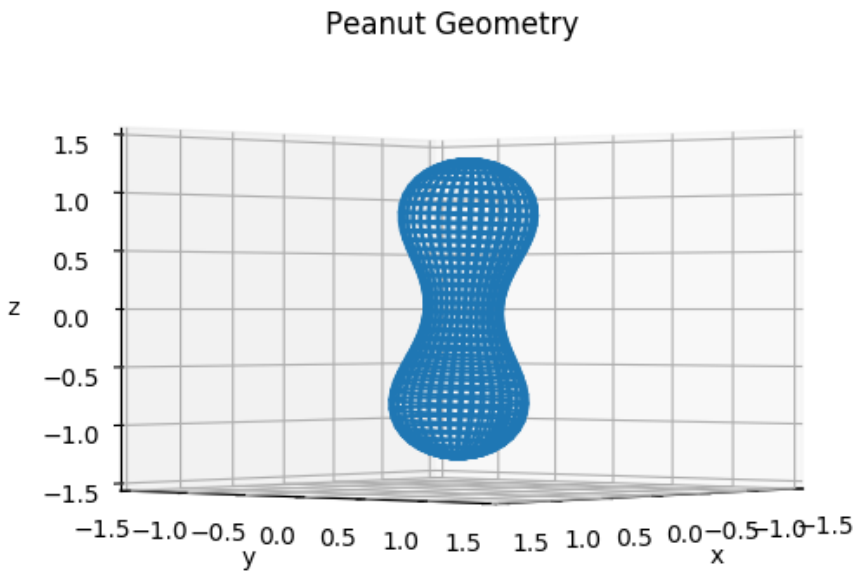

FIGURE 4.1: Embedding diagram for a peanut diagram, found numerically.

confidence in the accuracy of our embeddings. It is worth mentioning that while the lower the residual, the more accurate our results, the error of the embedding is accurately presented as R divided by the surface area of the original surface, given by $\int\int \sqrt{G_{\theta\theta}G_{\phi\phi} - G_{\theta\phi}^2} d\theta d\phi$. For a black hole of mass 1 and radius 2, the surface area would be 16π.

The metric for a zero charge, rotating black hole is given by

$$ds^2 = \Sigma d\theta^2 + \sin^2(\theta)[r^2 + a^2 + \frac{2Mra^2}{\Sigma}\sin^2\theta]d\phi^2, \tag{4.5}$$

where

$$\Sigma = r^2 + a^2\cos^2(\theta), r = M \pm \sqrt{M^2 - a^2}, a = \frac{J}{Mc}.$$

In figure 4.3 we have plotted the surfaces we find for various values of the angular momentum parameter a. In these plots we not only observe the dipping of the poles, but also the shrinking of the size of the black hole. One would initially

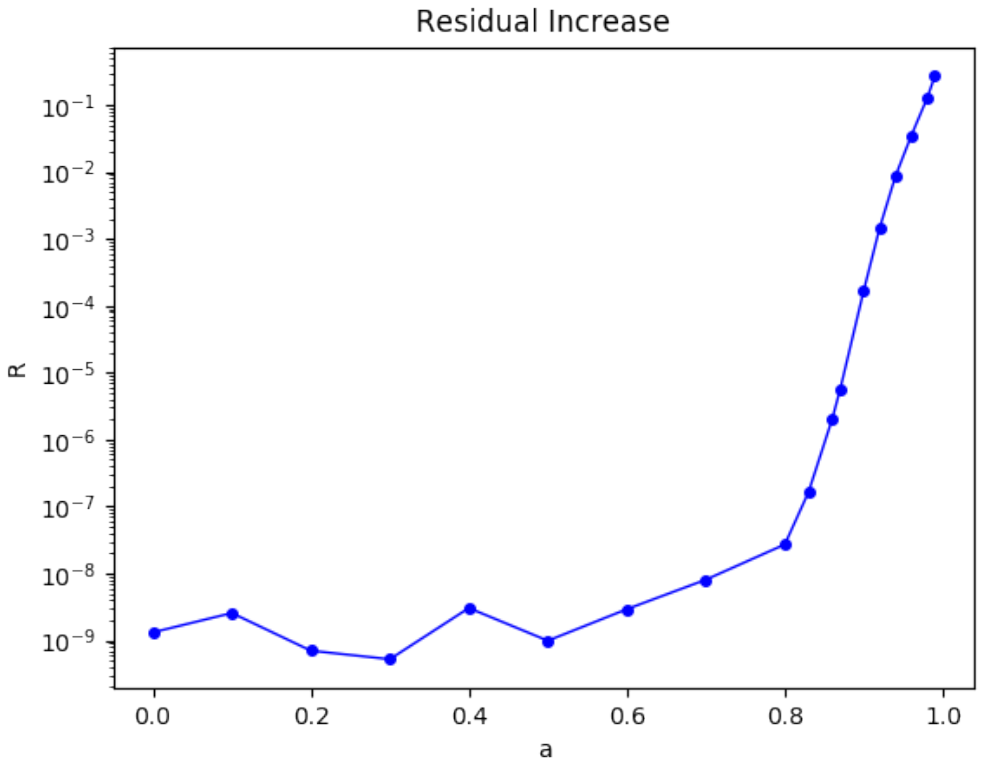

FIGURE 4.2: Semi-log plot of R for various values of a. After $a = \sqrt{3}/2$ R increases exponentially.

guess that surface area might be a conserved quantity in this system, but it is a straight forward derivation to show that if the total mass of the black hole stays constant, which we know it does, then the surface area of the black hole and its angular momentum are inversely proportional. This then explains the flattening of the black hole as a is increased.

While the surface area does decrease, the circumference along the equator, points which are co-rotating with the black hole, does not. This can be shown from the line element given in equation 4.5. Taking a line integral along the equator, because we are only considering points on this path, $d\theta = 0$, we have $ds^2 = G_{\phi\phi}d\phi^2$, giving

$$C = \int_0^{2\pi} \sqrt{G_{\phi\phi}}d\phi. \tag{4.6}$$

Computing this value, we find that $C = 4\pi$, for a black hole of mass equal to 1, in geometerized units. This means that the results of our test are in fact valid, showing a constant radius and circumference with decreasing surface area.

This result is unexpected but not surprising. Indeed, for a spinning sphere made of a soft material, as its angular momentum increases the centrifugal force felt at points along the equator causes the sphere to move outwards, causing a bulge. Since nothing else has changed, the surface area of the sphere must stay the same, requiring the poles to move towards the sphere's center, and thus having the circumference increase. The geometry of the Kerr spacetime on the other hand does not preserve surface area, but instead preserves circumference. This is due to the curvature of the Kerr spacetime.

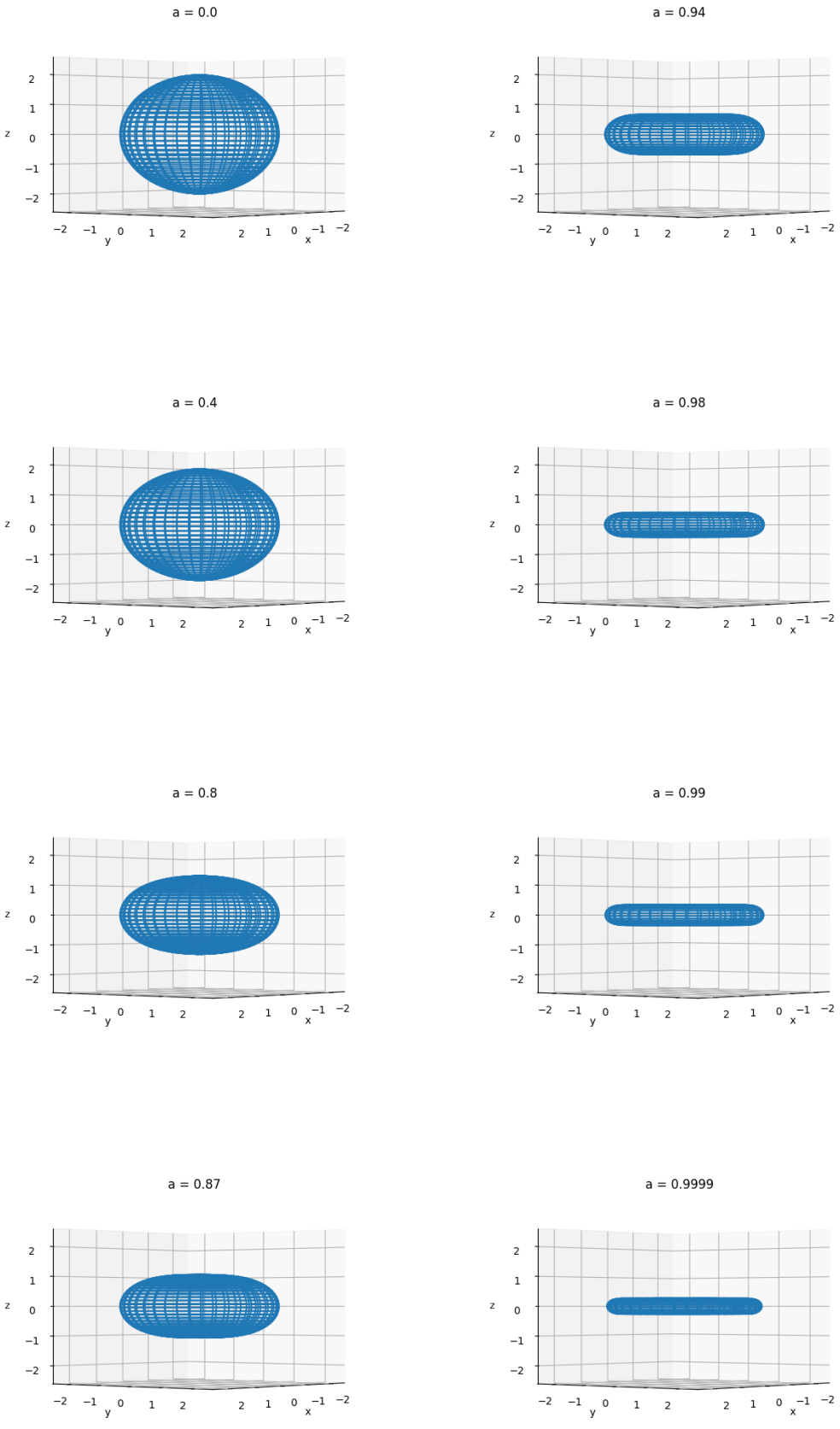

FIGURE 4.3: Plots of zero charge, rotating black holes at different values of the angular-momentum parameter a, at side view.

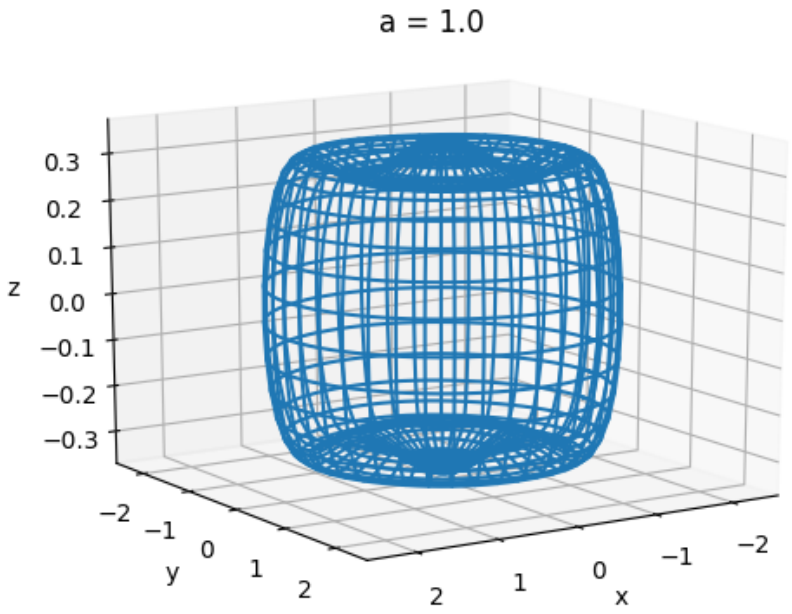

FIGURE 4.4: Plot of the embedding of a black hole with its angular momentum equal to 1. The poles are dip shaped because those regions cannot be embedded in Euclidean space.

Chapter 5

Results

Using our algorithm, we found embeddings for data from a numerical simulation of the ringdown of a black hole resulting from the merger of two smaller holes. This is the simulation run first by members of the SXS collaboration [3] to identify the details of the first ever detected black hole merger, now known as GW150914, having the same mass and spin parameters [2]. The simulation was run using the Spectral Einstein Code [3]. Embeddings were found for the horizon that exist just after the two black holes had formed. We were then able to verify the results of our embeddings visually, as they showed the non-axisymmetrical shape that results after the merger event occurs, and frame by frame we were able to confirm that the shape approaches that of an oblate spheroid, confirming the results of [9]. Two of the embeddings found are displayed in figure 5.1.

While the embeddings do confirm our expectations for the evolution of the system, we must note that the final residual remains larger than we would have expected from test cases. This may be related to a peculiar qualitative feature: a small bulge orbiting around the poles in a manner different than one would intuitively expect, when playing the embeddings frame by frame. We have not yet determined why the residuals are so large, or the uncertainties associated with the embeddings, but these are topics of interest to be pursued in the future. Also, at the time of writing, we chose to only use 300 parameters, but in principle the residual could be improved if we ran algorithm using more parameters.

A working version of the code can be found at `https://github.com/tpierrej`

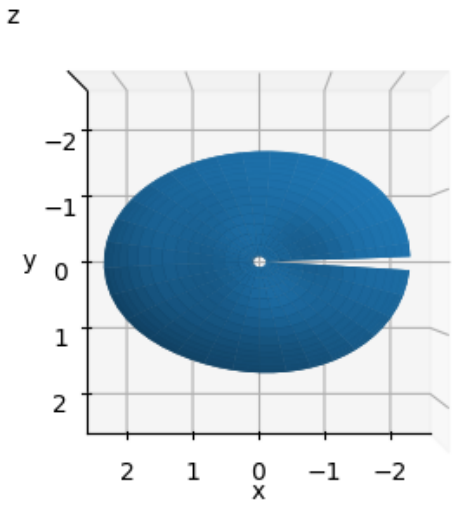

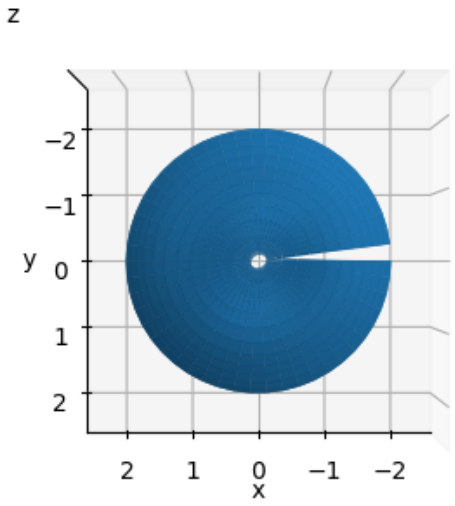

FIGURE 5.1: Top view plots for the embeddings of the simulated data. The top plot is just after the black holes begin to have a common horizon, while the bottom plot is 1461 time steps after. The missing pieces of the surfaces in the plots are artifacts from the coarseness of grid points from the computed data, i.e. the slice represents $\delta\phi$

Chapter 6

Discussion and Future Work

Embeddings allow for a direct and intuitive visualization of geometrical structure. Using them can provide us with insight into the dynamics of black holes and the curvature of spacetime that exists outside of them. In general, however, they are difficult to produce, especially when axisymmetry is not present. To overcome this we have posed the problem as an optimization problem, numerically solving for a global minimum that represents an accurate embedding of the surface in the Cartesian coordinates of a Euclidean geometry.

In our work we have expanded upon the work of Bondarescu et al. to produce code that numerically constructs embedding diagrams of general surfaces with spherical topology. The most obvious applications of our work is visualizing the black hole horizons that arise in numerical relativity data. We have tested this code in a variety of simple cases, and applied it to actual data from the Spectral Einstein Code [3]. While the application of our code to the computed data yielded residuals that were not as low as we would have liked, the visualizations still presented results that were reasonable, namely the settling down of the final object to a rotating black hole.

In the future, work may be done to move all our code into C or C++ code for further optimizations, as well as research into other optimization methods. Optimization is a large field with a vast collection of optimization algorithms, so it would be of interest to find one that performed better than the Truncated Newton method that was used here. Work may also be done to compute the quasilocal energy of dynamical black holes [7], which would make it possible to test basic conjectures about gravitational collapse, such as the hoop conjecture.

Bibliography

[1] Mihai Bondarescu, Miguel Alcubierre, and Edward Seidel. Isometric embeddings of black hole horizons in three-dimensional flat space. *Class. Quant. Grav.*, 19:375–392, 2002.

[2] B. P. Abbott et al. Observation of gravitational waves from a binary black hole merger. *Phys. Rev. Lett.*, 116:061102, Feb 2016.

[3] Spectral einstein code. https://www.black-holes.org/code/SpEC.html#publications-2000. Accessed: 3/29/2018.

[4] Reimann. https://www.maths.tcd.ie/pub/HistMath/People/Riemann/Geom/. Accessed: 3/30/2018.

[5] C.W. Misner, K.S. Thorne, and J.A. Wheeler. *Gravitation*. Number pt. 3 in Gravitation. W. H. Freeman, 1973.

[6] Larry Smarr. Surface geometry of charged rotating black holes. *Phys. Rev. D*, 7:289–295, Jan 1973.

[7] J. David Brown and James W. York, Jr. Quasilocal energy and conserved charges derived from the gravitational action. *Phys. Rev.*, D47:1407–1419, 1993.

[8] J.A. Wheeler and J.R. Klauder. *Magic Without Magic: John Archibald Wheeler: A Collection of Essays in Honor of His Sixtieth Birthday*. W. H. Freeman, 1972.

[9] Robert Owen. The Final Remnant of Binary Black Hole Mergers: Multipolar Analysis. *Phys. Rev.*, D80:084012, 2009.

[10] Gaussian curvature. https://en.wikipedia.org/wiki/Gaussian_curvature. Accessed: 3/29/2018.

[11] Joseph D Romano and Richard H Price. Embedding initial data for black-hole collisions. *Classical and Quantum Gravity*, 12(3):875, 1995.

[12] William H. Press, Saul A. Teukolsky, William T. Vetterling, and Brian P. Flannery. *Numerical Recipes in C (2Nd Ed.): The Art of Scientific Computing*. Cambridge University Press, New York, NY, USA, 1992.

[13] Stephen G. Nash. A survey of truncated-newton methods. *Journal of Computational and Applied Mathematics*, 124(1):45 – 59, 2000. Numerical Analysis 2000. Vol. IV: Optimization and Nonlinear Equations.

[14] Stephen G. Nash and Jorge Nocedal. A numerical study of the limited memory bfgs method and the truncated-newton method for large scale optimization. *SIAM Journal on Optimization*, 1:358–372, 1991.

[15] Stephen G. Nash and Jorge Nocedal. A numerical study of the limited memory bfgs method and the truncated-newton method for large scale optimization. *SIAM Journal on Optimization*, 1(3):358–372, 1991.

[16] J.B. Hartle. *Gravity: An Introduction to Einstein's General Relativity*. Addison-Wesley, 2003.